

Persistent homology-based explicit topological control for 2D topology optimization with MMA

Gengchen Li^{a,1}, Depeng Gao^{a,1}, Wenliang Yin^a, Hongwei Lin^{a,*}

^a*School of Mathematical Sciences, Zhejiang University, Hangzhou, 310058, China*

Abstract

Controlling structural complexity, particularly the number of holes, remains a fundamental challenge in topology optimization, with significant implications for both theoretical analysis and manufacturability. Most existing approaches rely on indirect strategies, such as filtering techniques, minimum length-scale control, or specific level-set initializations, which influence topology only implicitly and do not allow precise regulation of topological features. In this work, we propose an explicit and differentiable topology-control framework by integrating persistent homology into the classical minimum-compliance topology optimization problem. The design domain and density field are represented using non-uniform rational B-splines (NURBS), while persistence diagrams are employed to rigorously and quantitatively characterize topological features. Given a prescribed number of holes, a differentiable topology-aware objective is constructed from the persistence pairs and incorporated into the compliance objective, leading to a unified optimization formulation. The resulting problem is efficiently solved using the method of moving asymptotes (MMA). Numerical experiments demonstrate that the proposed approach enables explicit control over structural connectivity and the number of holes, thereby providing a systematic and mathematically grounded strategy for topology regulation.

Keywords: Topology optimization, Explicit topology control, Persistent homology, NURBS representation, MMA

1. Introduction

Topology optimization ([Bendsøe and Kikuchi, 1988](#)), first introduced by Bendsøe and Kikuchi, has evolved into a powerful design paradigm for determining optimal material distributions within prescribed domains to achieve superior structural performance. It has been widely adopted across numerous engineering applications. Despite these advances, several challenges remain, among which the control of structural complexity is of particular importance ([Zuo et al., 2022](#)).

*Corresponding author.

Email address: hwlin@zju.edu.cn (Hongwei Lin)

¹These authors contribute equally to this study.

Structural complexity is particularly critical from both theoretical and practical perspectives. From a theoretical standpoint, continuum topology optimization is known to be ill-posed, as the global optimum may contain infinitely many holes (Sigmund and Petersson, 1998). Imposing constraints on the number of holes regularizes the problem and contributes to restoring well-posedness. From a manufacturing perspective, excessively complex designs are often difficult or even infeasible to fabricate using conventional processes. Although additive manufacturing alleviates some of these limitations, certain technologies, such as selective laser sintering and fused deposition modeling, still prohibit the fabrication of enclosed internal cavities. Consequently, controlling the number of holes is essential for ensuring manufacturability and maintaining structural reliability.

Existing approaches for controlling structural complexity can generally be classified into implicit or explicit strategies. Implicit methods do not directly regulate the number of holes, but instead influence topology indirectly through auxiliary mechanisms. For instance, sensitivity and density filters (Bourdin, 2001, Sigmund, 1994) reduce numerous small holes as a by-product while suppressing checkerboard patterns. Geometric constraints (Zhou et al., 2015) restrict the minimum feature size rather than explicitly controlling the number of holes. The classical level-set method typically reduces the number of holes monotonically, making the final topology strongly dependent on the initial configuration (Wang et al., 2003). Virtual temperature approaches (Liu et al., 2015, Yamada and Noguchi, 2022, Li et al., 2018) can enforce structural connectivity but lack an explicit relationship between the control variables and the resulting number of holes. Consequently, these methods offer limited precision in topology control.

In contrast, explicit approaches aim to establish a direct relationship between the number of holes and the design variables. The moving morphable component method (MMC) (Zhang et al., 2017b) enables direct manipulation of holes through geometric components, while skeleton-based level-set formulations (Zhang et al., 2017a) assign an independent level-set function to each hole. Discrete counting formulas, such as the digital Gauss–Bonnet relation (Han et al., 2021), as well as graph-theory-inspired approaches (Zhao et al., 2020), have also been incorporated into BESO-type frameworks.

In this paper, we develop a persistent-homology-based framework that enables explicit and differentiable control of structural topology within a density-based optimization setting. Persistent homology provides a rigorous mathematical tool for quantifying topological features, allowing holes and connectivity to be measured directly and incorporated into the optimization process. By constructing differentiable objectives from persistence diagrams, the proposed method can be seamlessly integrated into gradient-based solvers, such as MMA. (Svanberg, 1987). To summarize, the main contributions of this work are as follows:

- An explicit topology-control strategy based on persistent homology that accurately captures and regulates the number of holes and connectivity.
- A differentiable persistence-based objective that integrates naturally with compliance minimization and enables efficient gradient-based optimization.
- A scalable framework that is readily extendable to three-dimensional topology opti-

mization.

The remainder of this paper is organized as follows. In Section 2, NURBS representation and the preliminaries on persistent homology are introduced. The topology control method based on persistent homology is presented in Section 3. In Section 4, the experimental results are presented to validate our proposed method. Finally, Section 5 concludes this study.

2. Preliminaries

2.1. NURBS representation

In isogeometric analysis (IGA), the same basis functions are employed for both geometric modeling and numerical analysis, enabling seamless integration between computer-aided design (CAD) and computer-aided engineering (CAE). Non-uniform rational B-splines (NURBS) are among the most widely used representations in CAD due to their ability to exactly describe common engineering geometries such as conic sections and free-form surfaces.

Let $\{\xi_1, \dots, \xi_{n+p+1}\}$ be a non-decreasing sequence of real numbers, referred to as a knot vector. Here, p denotes the degree of the B-spline basis functions, and n represents the number of basis functions. A knot vector is called uniform if its knots are equally spaced. An open uniform knot vector is a uniform knot vector with $p+1$ repeated knots at each end. In the following analysis and experiments, open uniform knot vectors are employed throughout.

A univariate B-spline basis function is defined recursively. For $p = 0$:

$$N_{i,0}(\xi) = \begin{cases} 1, & \text{if } \xi_i \leq \xi < \xi_{i+1}, \\ 0, & \text{otherwise.} \end{cases}$$

For $p > 0$:

$$N_{i,p}(\xi) = \frac{\xi - \xi_i}{\xi_{i+p} - \xi_i} N_{i,p-1}(\xi) + \frac{\xi_{i+p+1} - \xi}{\xi_{i+p+1} - \xi_{i+1}} N_{i+1,p-1}(\xi). \quad (1)$$

The NURBS basis function of degree p is defined as

$$R_{i,p}(\xi) = \frac{N_{i,p}(\xi)\omega_i}{\sum_{i'=1}^n N_{i',p}(\xi)\omega_{i'}},$$

where ω_i is the weight associated with the B-spline basis function $N_{i,p}(\xi)$.

A NURBS curve of degree p is defined as

$$C(u) = \sum_{i=0}^n \frac{\omega_i N_{i,p}(u) P_i}{\sum_{i'=0}^n \omega_{i'} N_{i',p}(u)}, \quad (2)$$

where P_i , $i \in \{0, 1, \dots, n\}$, are the control points, and ω_i , $i \in \{0, 1, \dots, n\}$ are the corresponding weights (Piegl and Tiller, 2012).

Higher-dimensional extensions of these spline concepts are constructed via tensor products. For example, a bivariate NURBS surface of degree (p, q) is defined as:

$$S(u, v) = \sum_{i=0}^m \sum_{j=0}^n \frac{\omega_{i,j} N_{i,p}(u) N_{j,q}(v) P_{i,j}}{\sum_{i'=0}^m \sum_{j'=0}^n \omega_{i',j'} N_{i',p}(u) N_{j',q}(v)}, \quad (3)$$

where $P_{i,j}$, $i \in \{0, 1, \dots, m\}$, $j \in \{0, 1, \dots, n\}$ are the control points in the u , v directions, respectively; $N_{i,p}(u)$, $N_{j,q}(v)$ are the B-spline basis functions of degree p and q in the corresponding parametric directions (Piegls and Tiller, 2012). In this paper, the structural geometry is represented by a bivariate tensor-product NURBS surface.

2.2. Persistent homology of cubical complex

Persistent homology is a fundamental tool in Topological Data Analysis (TDA) for extracting topological features of datasets filtered by real-valued functions. To characterize the topology of the structure under consideration, the continuous density field is discretized, thereby inducing a well-defined topological representation. In the two-dimensional setting, the discretized density field naturally results in image-like data. For such image-based representations, the cubical complex provides a particularly suitable computational framework.

In Euclidean space, an elementary interval is defined as $I = [l, l + 1]$, where $l \in \mathbb{Z}$. A k -cube σ^k is defined as the Cartesian product of k elementary intervals, such as points (0-cubes), segments (1-cubes), and squares (2-cubes). A face of a cube is a subset $F \subset I^k$ of the form $F = \prod_{i=1}^k J_i$ where J_i is either $\{l\}$, $\{l + 1\}$, or $[l, l + 1]$ for all $1 \leq i \leq k$. We denote $\tau \leq \sigma^k$ if τ is a face of σ^k . A cubical complex \mathcal{K} is a collection of k -cubes, such that each face of each cube in \mathcal{K} is also contained in \mathcal{K} . The union of all cubes in \mathcal{K} forms its underlying space \mathcal{S} . Fig. 1 shows examples of cubical complexes.

In general, the topological features of a cubical complex can be classified according to their dimension, namely connected components, one-dimensional loops (holes) and voids corresponding to $\dim = 0, 1, 2$, respectively. For two-dimensional topology optimization problems, the structural topology is fully characterized by connected components and one-dimensional loops. More precisely, zero-dimensional topological features correspond to the connected components of the structure, whereas one-dimensional features represent the holes within the structure. From the perspective of algebraic topology, these features are formally described by homology groups. For a cubical complex (\mathcal{K}) , its d th homology group $H_d(\mathcal{K})$ encodes the d -dimensional topological features mentioned above. The rank of $H_d(\mathcal{K})$, denoted by $\beta_d(\mathcal{K})$, is called the d -th Betti number and represents the number of independent d -dimensional homological features in (\mathcal{K}) . For example, $\beta_0(\mathcal{K})$ equals the number of connected components of \mathcal{K} while $\beta_1(\mathcal{K})$ corresponds to the number of independent one-dimensional loops (i.e., holes).

Topological features defined on discrete structures cannot be directly optimized using conventional discrete metrics. To address this limitation, persistent homology is introduced, enabling the tracking of the birth and death of topological features along a sequence of nested complexes, known as a filtration. A filtration is constructed from a function defined on a cubical complex $f : \mathcal{K} \rightarrow \mathbb{R}$, by considering its sublevel sets. Let $f : \mathcal{K} \rightarrow \mathbb{R}$ be a function

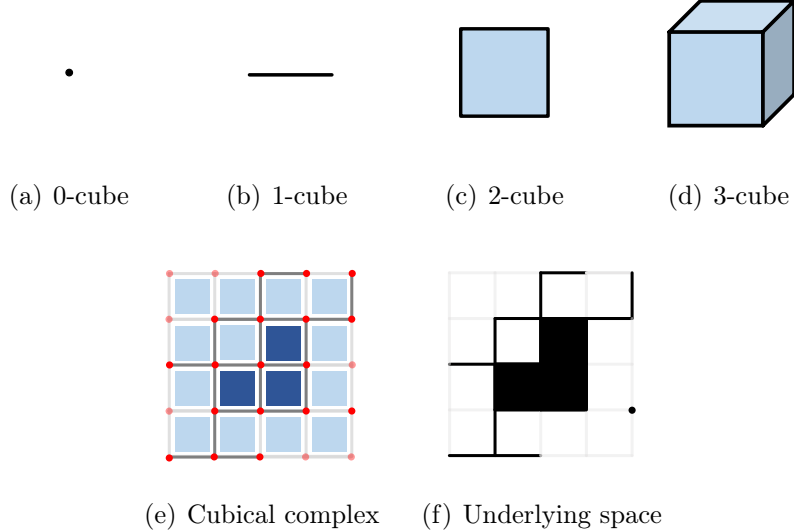


Figure 1: Cubical complex. (a)-(d) Examples of k -dimensional cubes. (e) An example of cubical complex represented by dark part, which is a collection of cubes. (f) The underlying space constructed from (e) by merging all cubes as a topological space on the plane.

defined on all elementary cubes of \mathcal{K} that satisfies: $\forall \sigma \in \mathcal{K}, \forall \tau \leq \sigma, f(\tau) \leq f(\sigma)$. Then, for any $a \in \mathbb{R}$, the sublevel set of \mathcal{K} with respect to f is defined as $\mathcal{K}(f, a) = f^{-1}((-\infty, a])$. For a series of $a_0 \leq a_1 \leq \dots \leq a_t$, we have

$$\mathcal{K}(f, a_0) \subseteq \mathcal{K}(f, a_1) \subseteq \dots \subseteq \mathcal{K}(f, a_t)$$

The sublevel filtration \mathcal{F} is defined as a nested sequence of cubical complexes $\mathcal{K}(f, a_0) \subseteq \mathcal{K}(f, a_1) \subseteq \dots \subseteq \mathcal{K}(f, a_t)$, where the threshold parameter satisfies $a_0 \leq a_1 \leq \dots \leq a_t$. As the parameter a_t increases, the emergence (birth) and disappearance (death) of topological features in different dimensions can be systematically tracked. The filtration therefore reveals the multi-scale topological structure underlying the data. Persistent homology computes not only the homology group of each complex in the filtration but also records the birth and death times of topological features according to well-defined algebraic rules (Edelsbrunner and Harer, 2010). Through this framework, topological characteristics are encoded as continuous variables instead of discrete Betti numbers, thereby enabling gradient-based optimization of topology. The lifespan of each topological feature can be visualized as an interval along the filtration parameter axis, forming what is known as a persistence barcode. Specifically, if a topological feature appears in $\mathcal{K}(f, b)$ and disappears in $\mathcal{K}(f, d)$, it is represented as a persistent pair (b, d) . These persistent pairs (b_i, d_i) can equivalently be mapped to points (b_i, d_i) in the Cartesian plane, yielding a persistence diagram (PD), which is one of the most widely used representations in TDA. Fig. 2 illustrates the persistent pairs (b_i, d_i) represent these topological features and can be plotted into a persistence diagram or a persistence barcode.

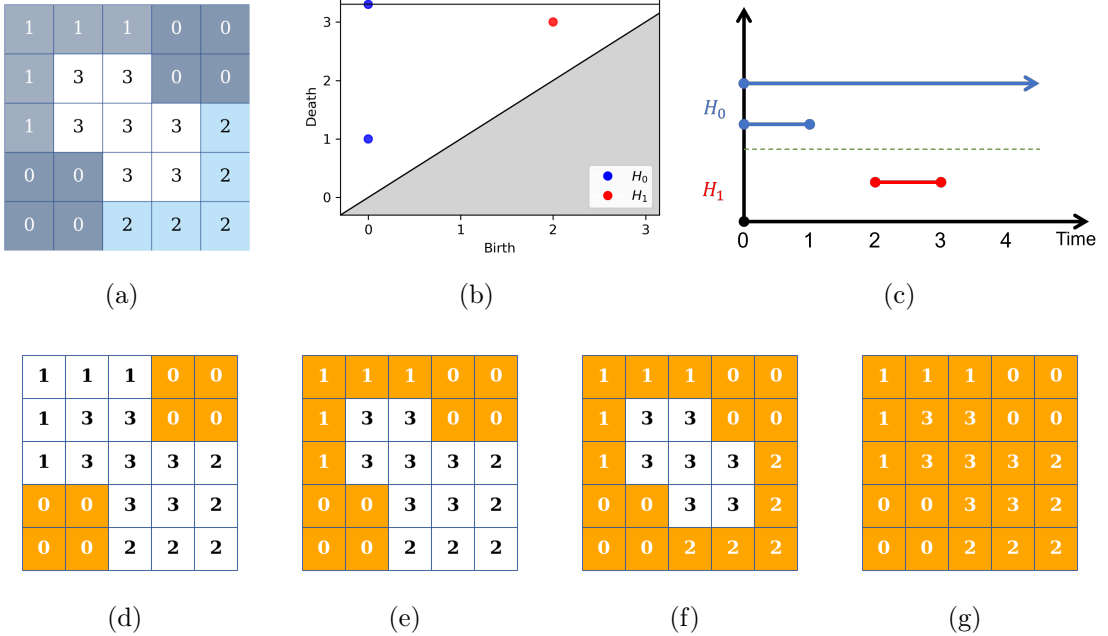


Figure 2: Filtration on a cubical complex. (a) is a cubical data with height function values on its grid cells. (d)–(g) show the corresponding filtration of (a) and each item of this filtration is a cubical complex which represents the sublevel set of original cubical data. The topological features can be extracted from those expanding cubical complexes with threshold value increasing. Using persistent homology, one can obtain the persistence diagram (b) and persistence barcode (c) of filtration (d)–(g).

3. Methodology

3.1. Topology control via persistent homology

PD provides a compact and rigorous representation of the topological characteristics of a structure, thereby enabling modifications of the underlying topology through its optimization. Within this framework, the PD is optimized via gradient-descent methods (Poulenard et al., 2018). Subsequent theoretical studies have rigorously established the correctness and convergence properties of persistence-based optimization schemes and have demonstrated that a broad class of persistence-based functions can be optimized using stochastic subgradient descent algorithms (Carriere et al., 2021). Moreover, persistence-based optimization of PDs through gradient descent has shown significant effectiveness across a wide range of applications (Clough et al., 2020).

3.1.1. Filtration induced by density field

Let ρ be a density field represented by NURBS:

$$\rho(u, v) = \sum_{i=0}^m \sum_{j=0}^n \frac{\omega_{i,j} N_{i,p}(u) N_{j,q}(v) P_{i,j}}{\sum_{i'=0}^m \sum_{j'=0}^n \omega_{i',j'} N_{i',p}(u) N_{j',q}(v)}, \quad (4)$$

For the binarized structure

$$\tilde{\rho} = \begin{cases} 1, & \rho \geq \bar{\rho} \\ 0, & \rho < \bar{\rho} \end{cases} \quad (5)$$

where $\bar{\rho}$ is the threshold, and the sublevel filtration can be induced by employing the equivalent structural representation $-\rho \leq -\bar{\rho}$. Therefore, by substituting the filtration function f with $-\rho$, computing the cubical complexes of the discretized density field, and applying the sublevel filtration mentioned above, the topological features of the structure can be obtained. Suppose the resulting k -dimensional persistence diagrams consist of the following persistence pairs:

$$P_k = \{b_{i,k}, d_{i,k}\}_{i=0}^{N_k-1}, \quad (6)$$

where $b_{i,k}$ and $d_{i,k}$ are the birth and death times of the i -th persistence pair in dimension k . As shown in Fig. 3, only those persistence pairs born before $-\bar{\rho}$ and die after $-\bar{\rho}$ (i.e., persistence pairs located in regions I and II) correspond to topological features present in the structure. Based on this correspondence between persistence pairs and topological features, the topology of the structure can be controlled by optimizing the PD. The key to persistence-based optimization is to find a correspondence between underlying complex and persistence pairs, that is, (b_i, d_i) . Let $f : \mathcal{K} \rightarrow \mathbb{R}$ be a function on all elementary cubes in \mathcal{K} such that it generates a filtration \mathcal{F} . Every homology generator gives birth at an elementary cube τ_i and dies at another elementary cube σ_i . Thus, persistence pair (b_i, d_i) can be written as $(f_{\tau_i}, f_{\sigma_i})$. Suppose $\{c_j\}$ are the parameters to be optimized, we can replace gradient $\frac{\partial b_i}{\partial c_j}$ and $\frac{\partial d_i}{\partial c_j}$ with $\frac{\partial f_{\tau_i}}{\partial c_j}$ and $\frac{\partial f_{\sigma_i}}{\partial c_j}$ due to the invariance of critical elementary cubes within a local parameter neighborhood.

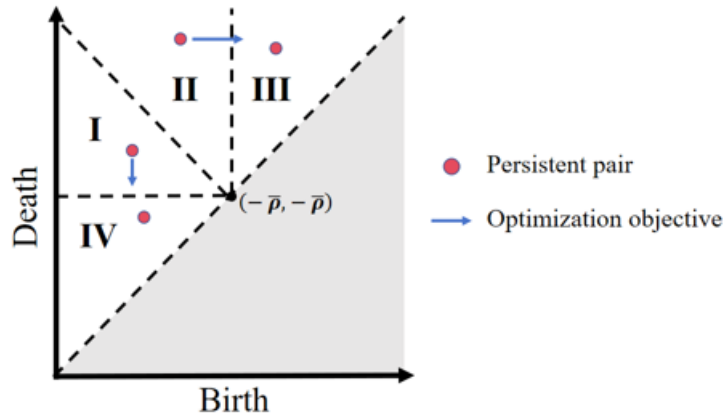


Figure 3: A two-dimensional persistence diagram. Regions I, II, III, and IV are segmented by lines $y = -x$, $x = -\bar{\rho}$ and $y = -\bar{\rho}$. The persistence pairs in regions I and II correspond to the isolated holes within the binarized structure. The blue arrows indicate the direction of the optimization objective.

3.1.2. Zero-dimensional topology objective function

The presence of extra connected components may affect manufacturability. Therefore, we should design a zero-dimensional topology objective function to ensure the structural connectivity. A two-dimensional PD as shown in Fig. 3 is utilized to illustrate the persistence-based optimization. Since the death times of the topological features are always larger than their birth times, all persistence pairs in the PD are located above the line $y = x$. The diagram is segmented by the lines $y = x$, $x = -\bar{\rho}$, $y = -\bar{\rho}$ and $y = -x$ into four regions. In 0-dimensional situations, the set $\{-\rho \leq +\infty\}$ is always one connected component, which corresponds to a persistent pair $(b, +\infty)$, $b \in \mathbb{R}$ in the zero-dimensional persistence diagram. To ensure no additional connected components exist in the structure, our optimization objective is to eliminate persistent pairs in regions I and II of the zero-dimensional PD. Excess persistence pairs located in regions I and II should be removed and translocated to regions III and IV. Specifically, persistence pairs in region I are translocated to region IV, and persistence pairs in region II are translocated to region III to avoid a significant structure change caused by a considerable movement of persistence pairs.

The 0-dimensional persistence pairs P_0 defined in Eq. (6) are categorized into distinct sets based on regions.

$$\begin{cases} P_0^I = \{(b_{i,0}^I, d_{i,0}^I)\}_{i=0}^{N_0^I-1} \\ P_0^{II} = \{(b_{i,0}^{II}, d_{i,0}^{II})\}_{i=0}^{N_0^{II}-1}, \end{cases} \quad (7)$$

where N_0^I and N_0^{II} denote the counts of persistence pairs within regions I and II, respectively. The repositioning of 0-dimensional persistence pairs from region I to IV and region II to III, respectively, is achieved by defining the objective function as

$$C_{top}^0 = \sum_{i=0}^{N_0^I-1} d_{i,0}^I - \sum_{i=0}^{N_0^{II}-1} b_{i,0}^{II}. \quad (8)$$

3.1.3. One-dimensional topology objective function

To control the structural complexity, we impose a constraint on the maximum number of holes \bar{N}_1 in the structure. We design the objective function from a dual perspective: by treating the material as voids and voids as material. That is, inducing filtration on $\rho < \bar{\rho}$ to capture the holes. Increasing the threshold $\bar{\rho}$ naturally induces a corresponding filtration on the void phase. and then the holes in the structure can be captured by computing the 0-dimensional PD.

However, not all 0-dimensional persistence pairs represent structural holes. Only those that do not intersect the boundary of the design domain are regarded as holes. Therefore, after inducing the filtration, we employ topological inverse mapping to determine the birth locations of the 0-dimensional topological features in the parametric domain. In the discretized density field, a breadth-first search (BFS) is then performed from each birth location to check whether the corresponding component intersects the boundary of the design domain, thereby filtering out the actual structural holes.

We control the maximum number of holes in the structure. The number of holes N_1 is constrained not to exceed \bar{N}_1 . We can induce filtration based on $\rho < \bar{\rho}$ and obtain the corresponding 0-dimensional persistence pairs of holes through BFS:

$$\tilde{P}_0 = \{(\tilde{b}_{i,0}, \tilde{d}_{i,0})\}_{i=0}^{N_1-1}. \quad (9)$$

Suppose $\{(\tilde{b}_{i,0}, \tilde{d}_{i,0})\}_{i=0}^{N_1-1}$ are sorted in ascending order of area. The area of each hole is approximated by the number of discrete elements it contains. When $N_1 > \bar{N}_1$, we drive the first $N_1 - \bar{N}_1$ persistence pairs out of regions I and II. Similar to the zero-dimensional case, we categorize these $N_1 - \bar{N}_1$ persistence pairs into distinct sets based on their respective regions.

$$\begin{cases} \tilde{P}_0^I = \{(\tilde{b}_{i,0}^I, \tilde{d}_{i,0}^I)\}_{i=0}^{(N_1 - \bar{N}_1)^I - 1} \\ \tilde{P}_0^{II} = \{(\tilde{b}_{i,0}^{II}, \tilde{d}_{i,0}^{II})\}_{i=0}^{(N_1 - \bar{N}_1)^{II} - 1}, \end{cases} \quad (10)$$

where $(N_1 - \bar{N}_1)^I$ and $(N_1 - \bar{N}_1)^{II}$ denote the number of persistence pairs needed to be removed from regions I and II, respectively. Thus, one-dimensional topology objective function can be defined as:

$$C_{top}^1 = \sum_{i=0}^{(N_1 - \bar{N}_1)^I - 1} \tilde{d}_{i,0}^I - \sum_{i=0}^{(N_1 - \bar{N}_1)^{II} - 1} \tilde{b}_{i,0}^{II}. \quad (11)$$

3.2. Problem and formulation

The minimum compliance optimization problem with zero-dimensional and one-dimensional topological constraints can be summarized as follows:

$$\begin{aligned} \text{Find: } \rho &= \sum_{i=0}^m \sum_{j=0}^n \omega_{i,j} N_{i,p}(u) N_{j,q}(v) \rho_{i,j} \\ \text{Minimize: } C(\rho) &= \frac{1}{2} \mathbf{F}^T \mathbf{U} + C_{top}(\rho) \\ \text{Subject to: } V(\rho) &\leq V_0 \\ \mathbf{KU} &= \mathbf{F} \\ \rho_{min} &\leq \rho \leq 1, \end{aligned} \quad (12)$$

where $\rho_{i,j}$ are the design variables, denoting the control coefficients of the density field, $V(\rho)$ and V_0 represent the volume fraction of the optimized structure and a predefined threshold, respectively, and $\rho_{min} = 0.1$ is the lower bound of density to prevent singular stiffness matrices. Based on Eq. (8) and (11), topological objective function $C_{top}(\rho)$ is defined as follows:

$$C_{top}(\rho) = \mu_0 C_{top}^0 + \mu_1 C_{top}^1 \quad (13)$$

where μ_0 and μ_1 denote the weights of 0-dimensional and 1-dimensional topology objective functions, respectively.

3.3. Sensitivity analysis

In this section, we perform a sensitivity analysis of the objective function and the constraints with respect to the design variables.

The sensitivity of C_{top}^0 and C_{top}^1 with respect to $\rho_{i,j}$ are computed utilizing the topological inverse mapping (Poulenard et al., 2018, Brüel-Gabrielsson et al., 2020)

$$\pi_{\rho}(b_i, d_i) = (\pi_b(b_i), \pi_d(d_i)), \quad (14)$$

where (b_i, d_i) denotes a persistence pair, $\pi_b(b_i)$ and $\pi_d(d_i)$ denote the locations in the parameter domain that correspond to the birth and death of the topological feature, respectively. Based on the inverse mapping π_{ρ} and the differential chain rule, the partial derivatives of i -dimensional topological objective function with respect to the control coefficients of the density field can be derived:

$$\begin{aligned} \frac{\partial C_{top}^i}{\partial \rho_{i,j}} &= \frac{\partial C_{top}^i}{\partial b} \frac{\partial b}{\partial \rho_{i,j}} + \frac{\partial C_{top}^i}{\partial d} \frac{\partial d}{\partial \rho_{i,j}} \\ &= - \sum_{(b_i, d_i) \in I} \frac{\partial(-\rho)}{\partial \rho_{i,j}}(\pi_b(b_i)) + \sum_{(b_i, d_i) \in II} \frac{\partial(-\rho)}{\partial \rho_{i,j}}(\pi_d(d_i)) \\ &= \sum_{(b_i, d_i) \in I} \frac{\partial \rho}{\partial \rho_{i,j}}(\pi_b(b_i)) - \sum_{(b_i, d_i) \in II} \frac{\partial \rho}{\partial \rho_{i,j}}(\pi_d(d_i)) \end{aligned} \quad (15)$$

Then the sensitivity of the whole objective function is:

$$\begin{aligned} \frac{\partial C(\rho)}{\partial \rho_{i,j}} &= \frac{\partial \mathbf{U}^T \mathbf{K} \mathbf{U}}{2 \partial \rho_{i,j}} + \mu_0 \frac{\partial C_{top}^0}{\partial \rho_{i,j}} + \mu_1 \frac{\partial C_{top}^1}{\partial \rho_{i,j}} \\ &= -\frac{1}{2} p \rho^{p-1} \mathbf{U}^T \mathbf{K} \mathbf{U} \frac{\partial \rho}{\partial \rho_{i,j}} \\ &\quad + \sum_{i=0}^1 \mu_i \left[\left(\sum_{(b_i, d_i) \in I} \frac{\partial \rho}{\partial \rho_{i,j}}(\pi_b(b_i)) - \sum_{(b_i, d_i) \in II} \frac{\partial \rho}{\partial \rho_{i,j}}(\pi_d(d_i)) \right) \right]. \end{aligned} \quad (16)$$

The sensitivity of the volume constraint is given by:

$$\begin{aligned} \frac{\partial V(\rho)}{\partial \rho_{i,j}} &= \frac{\partial \int_{\Omega} \rho d\Omega}{\partial \rho_{i,j}} \\ &= \frac{\partial \int_{\Omega} \sum_{i=0}^m \sum_{j=0}^n \frac{\omega_{i,j} N_{i,p}(u) N_{j,q}(v) P_{i,j}}{\sum_{i'=0}^m \sum_{j'=0}^n \omega_{i',j'} N_{i',p}(u) N_{j',q}(v)} d\Omega}{\partial \rho_{i,j}} \\ &= \int_{\Omega} \frac{\omega_{i,j} N_{i,p}(u) N_{j,q}(v) P_{i,j}}{\sum_{i'=0}^m \sum_{j'=0}^n \omega_{i',j'} N_{i',p}(u) N_{j',q}(v)} d\Omega. \end{aligned} \quad (17)$$

3.4. Optimization algorithm

In summary, the proposed topology control method first employs the density field ρ to induce a sublevel filtration, yielding the corresponding zero-dimensional persistence pairs. To ensure the optimization stability, we control the number of holes also by optimizing the associated zero-dimensional topological features. By adopting a dual-phase strategy, ρ is used to induce sublevel filtration for hole detection. Topological inverse mapping combined with BFS is then employed to identify the holes in the structure, resulting in zero-dimensional persistence pairs corresponding to the void phase. When the prescribed topological constraints are violated, the persistence pairs associated with redundant connected components or excessive holes are optimized. Specifically, by minimizing their death times or maximizing their birth times, these undesired topological features are gradually eliminated from the structure.

Owing to the differentiability of the persistence-based objective function, the proposed framework can be seamlessly integrated into classical topology optimization procedures, enabling rigorous and continuous control of structural complexity. The overall optimization procedure is summarized in Algorithm 1:

Algorithm 1 Optimization algorithm with topology control

Input: Design domain represented by NURBS;

Boundary conditions;

Maximum number of holes \bar{N}_1 ;

Poisson's ratio, Young's modulus;

Volume fraction V_0 ;

Maximum number of iterations;

Output: Optimized density field represented by NURBS (4).

- 1: **while** the maximum number of iterations is not reached **do**
- 2: Perform finite element analysis, and compute the compliance and volume sensitivities;
- 3: Induce filtration on $-\rho < -\bar{\rho}$ and compute the number of connected components N_0 ;
- 4: Induce filtration on $\rho < \bar{\rho}$ and perform BFS in the parameter domain;
- 5: Compute the number of holes N_1 and sort them in ascending order of area;
- 6: **if** $N_0 > 1$ **or** $N_1 > \bar{N}_1$ **then**
- 7: Incorporate the topological objective function into the total objective function;
- 8: Compute the sensitivity of the augmented objective function;
- 9: **end if**
- 10: **if** $N_0 = 1$ **and** $N_1 \leq \bar{N}_1$ **and** excess material exists **then**
- 11: Freeze the density of the existing holes;
- 12: Compute the sensitivities to optimize the compliance of the remaining structure;
- 13: **end if**
- 14: Update the density control coefficients using MMA;
- 15: **end while**

4. Numerical examples

In this section, several benchmark examples are presented to validate the effectiveness of the proposed method. All problems are solved using MMA. The density field is represented by NURBS, and persistent homology is evaluated at each iteration to extract topological features of the structure. The results demonstrate that the proposed framework can explicitly ensure the structural connectivity and accurately control the number of holes.

Suppose the solid material has a Young's modulus of 1.9×10^{11} and Poisson's ratio of 0.3. The filtering radius of the sensitivity filter is $1.5h$, where h represents the element size. In this study, the threshold $\bar{\rho}$ is 0.4. The maximum iteration number is set to 400. Due to structural topology instability during the initial iterations, we implemented topology control starting from the 20 – 30th iteration in our experiments. Moreover, the density field discretization resolution for calculating persistent homology is set to 200×200 , and the corresponding parameter domain is $[0, 1]^2$. This resolution ensures that the structural topology information derived from the discrete density field remains consistent with the structure defined by the continuous density field.

4.1. Short beam example

In this example, the classical short beam problem shown in Fig. 4 is used to investigate the capability of the proposed method for topological control. The length of the beam is set to two times its width. The design domain is represented by a 61×61 bicubic NURBS surface. The left boundary of the design domain is fixed, and a downward force of $F = 10^5$ is applied at its lower-right corner. The classical minimum compliance problem without topology constraint is solved with $V_0 = 0.5$. As shown in Fig. 4(c), there exist 5 holes in the structure.

A topological constraint is imposed such that the number of holes in the optimized structure is no more than \bar{N}_1 , while guarantee its connectivity at the same time. Fig. 5 illustrates the optimized results for $\bar{N}_1 = 1, 2, 3, 4, 5$, and 6. It can be observed that our method successfully achieves effective control of the structural topology. Table 1 summarizes the compliance values, topology-control weights, and computational time for different prescribed maximum number of holes \bar{N}_1 . It can be observed that the compliance increases gradually as the allowable number of holes decreases. This trend is physically intuitive: restricting the number of holes reduces structural design freedom and limits the ability of the optimizer to distribute material in a compliance-optimal manner. Nevertheless, the compliance variation remains moderate, indicating that the proposed topology-control strategy achieves structural regularization with only a limited performance penalty.

Moreover, stricter topological constraints require larger weights for the topology objective function. When the target topology deviates significantly from the unconstrained solution, a stronger topological driving force is necessary to overcome the compliance-minimizing tendency of the optimization process. This observation confirms that the proposed persistence-based objective provides a controllable and tunable mechanism for balancing structural performance and topological complexity.

In addition, the optimized structures demonstrate smooth geometric transitions without artificial discontinuities. The structural connectivity is consistently preserved across all cases, confirming the effectiveness of the zero-dimensional topology control. When $\bar{N}_1 = 5$ or 6, the optimized structures are nearly identical to the unconstrained design, further validating that the proposed method does not introduce unnecessary distortions when the prescribed topology is already satisfied. These results demonstrate that the proposed framework enables explicit and reliable regulation of structural topology while maintaining competitive mechanical performance and numerical stability.

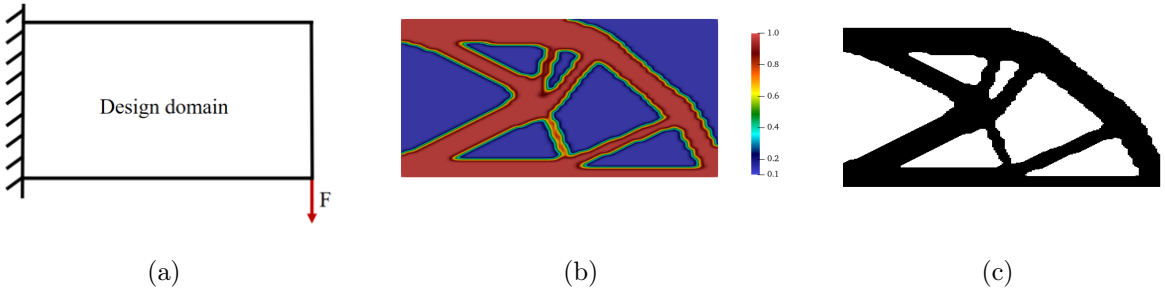


Figure 4: (a) The short beam model. (b) Optimization result without topology control. (c) Binary structure corresponding to the density field in (b).

Table 1: Comparison of compliance, number of holes, and time costs for the short beam benchmark under different topology-control settings.

	$\bar{N}_1 = 1$	$\bar{N}_1 = 2$	$\bar{N}_1 = 3$	$\bar{N}_1 = 4$	$\bar{N}_1 = 5$	$\bar{N}_1 = 6$
weights (μ_0, μ_1)	(0.8,0.6)	(0.1,0.1)	(0.8,0.6)	(0.1,0.1)	(0.1,0.1)	(0.1,0.1)
Compliance	5.01	4.95	4.91	4.91	4.90	4.89
Time (s)	445.3	440.2	423.2	422.1	418.6	412.3

Fig. 6 illustrates the evolution of the compliance and the binarized density structures during the optimization process under the constraint $\bar{N}_1 = 3$. As shown in Fig. 6(a), the compliance decreases rapidly within the first 30 iterations and then gradually stabilizes. This behavior indicates that achieving a stable structure requires approximately 30 iterations without topological control.

Figs. 6(b) - 6(f) depict the structural evolution and demonstrate the effectiveness of the proposed topological objective function. Fig. 6(c) shows that at the 17th iteration, the number of holes in the structure reaches 7, exceeding the prescribed maximum and thereby violating the topological constraint. After activating topology control, the number of holes is reduced to 4 by the 20th iteration (Fig. 6(d)), confirming that the persistence-based objective effectively suppresses redundant topological features. Compared with the configuration at the 17th iteration, several small holes within the structure are removed, indicating that

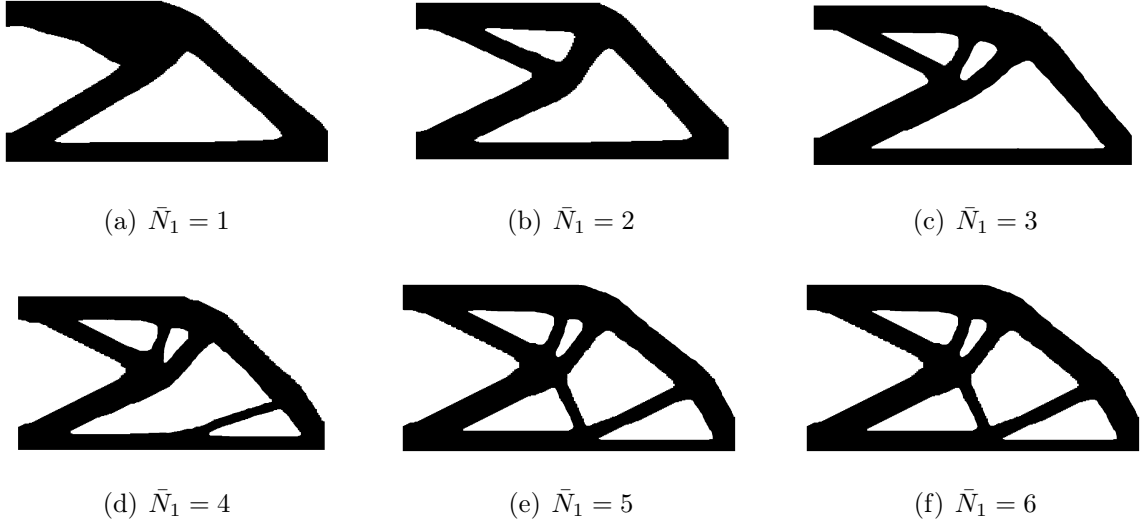


Figure 5: Optimization results of the short beam for $\bar{N}_1 = 1, 2, 3, 4, 5, 6$, respectively.

the optimization preferentially eliminates topologically insignificant holes. By the 30th iteration, the number of holes further decreases to 3, satisfying the prescribed constraint. This reduction is achieved through structural reconnection and merging of adjacent void regions, which alters the homological structure while preserving overall mechanical performance. The structural transitions occur smoothly without introducing numerical oscillations or instability in the compliance curve. Finally, at the 75th iteration, excess material is completely eliminated and the structure reaches a stable topology. The compliance remains nearly constant during the late stage of the optimization, demonstrating that the proposed topology-control mechanism does not compromise convergence stability.

4.2. L-shaped beam example

Fig. 7 presents the L-shaped beam benchmark. The design domain is represented by a 103×52 biquadratic NURBS surface. The top boundary of the domain is fully fixed, and a downward point load of $F = 10^5$ is applied, as illustrated in Fig. 7(a). The classical minimum compliance problem without topology constraint is solved with $V_0 = 0.5$. As shown in Figs. 7(b) and 7(c), there exist 6 holes in the structure without topological control.

We impose topological constraints on the maximum number of holes in the L-shaped beam and guarantee the structural connectivity. Fig. 8 shows the optimization results for $\bar{N}_1 = 1, 2, 3, 4, 5, 6, 7$. Table 2 reports the compliance values, topology-objective weights and computational time for $\bar{N}_1 = 1, 2, 3, 4, 5, 6, 7$. The results exhibit a clear performance-complexity trade-off: as \bar{N}_1 decreases, the compliance increases moderately, reflecting the reduced design freedom induced by stricter topological constraints. Meanwhile, tighter hole limits generally require larger topology weights (μ_0, μ_1), indicating that a stronger topological driving force is needed when the prescribed topology deviates substantially from the compliance-optimal unconstrained solution. When $\bar{N}_1 \geq 6$, the resulting structures are close to the

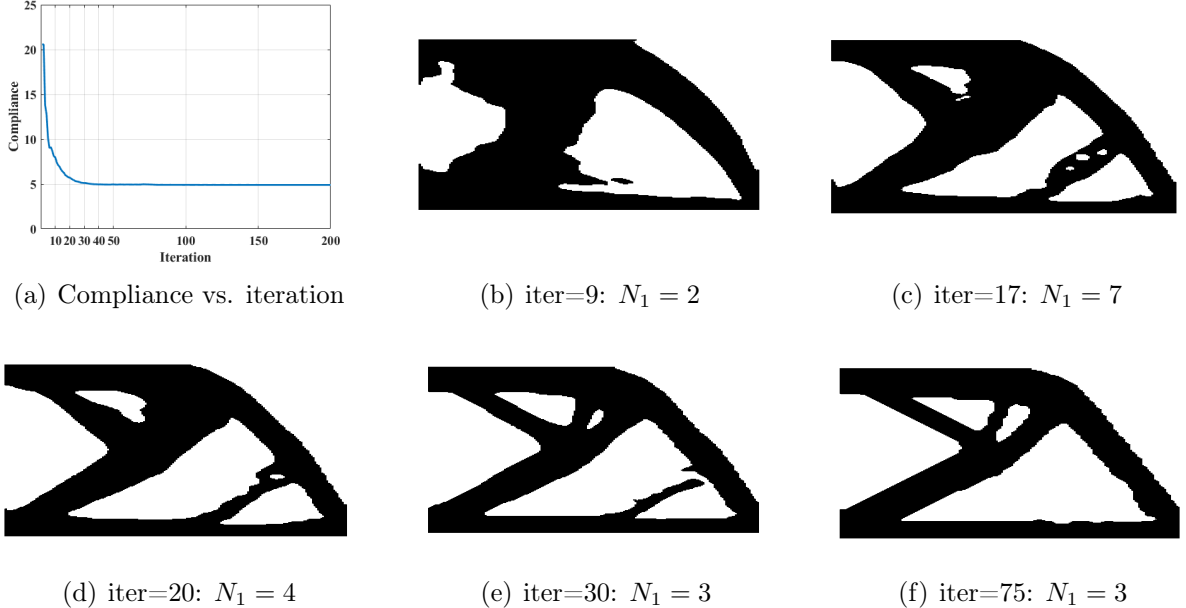


Figure 6: Evolution of the optimized topology for the short beam when $\bar{N}_1 = 3$. Binary density fields at representative iterations are shown. The proposed topology-control strategy progressively eliminates redundant holes and enforces the prescribed connectivity constraint.

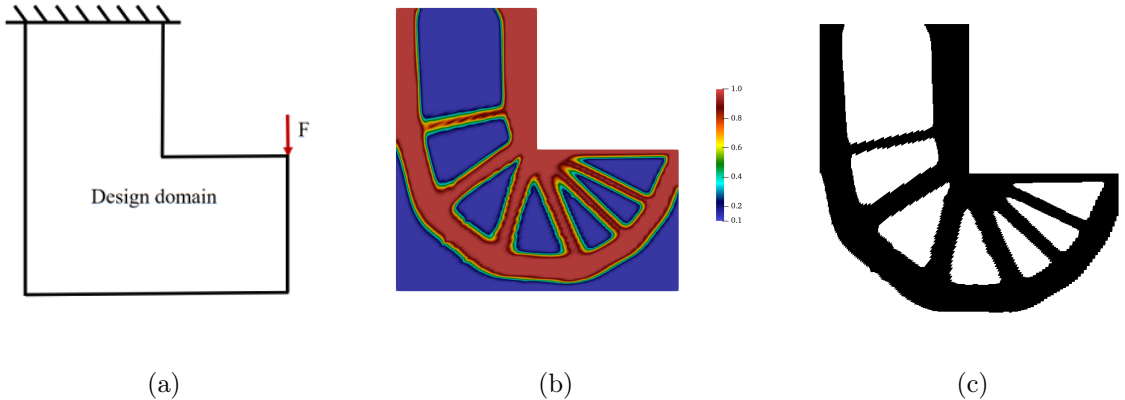


Figure 7: (a) L-shaped beam model. (b) Optimization result without topology control. (c) Binary structure corresponding to the density field in (b).

unconstrained design, confirming that the proposed method does not introduce unnecessary distortions once the target topology is already satisfied.

Fig. 9 illustrates the convergence behavior and topology evolution for the case $\bar{N}_1 = 4$. As shown in Fig. 9(a), the compliance decreases rapidly during the early iterations as the main load-carrying skeleton forms, and then remains stable. Importantly, although the compliance stabilizes, the topology continues to evolve under the influence of the topological

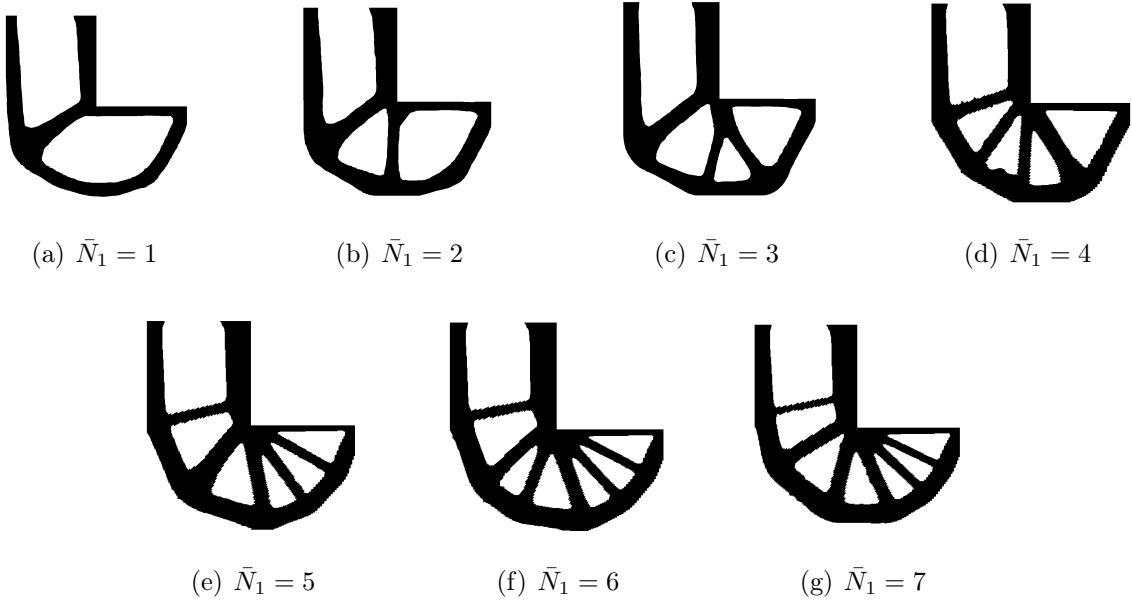


Figure 8: Optimization results of the L-shaped beam for $\bar{N}_1 = 1, 2, 3, 4, 5, 6, 7$, respectively.

Table 2: Comparison of compliance, number of holes, and time costs for the L-shaped beam benchmark under different topology-control settings.

	$\bar{N}_1 = 1$	$\bar{N}_1 = 2$	$\bar{N}_1 = 3$	$\bar{N}_1 = 4$	$\bar{N}_1 = 5$	$\bar{N}_1 = 6$	$\bar{N}_1 = 7$
weights (μ_0, μ_1)	(0.8,0.6)	(0.8,0.6)	(0.4,0.3)	(0.4,0.3)	(0.4,0.3)	(0.2,0.1)	(0.1,0.1)
Compliance	5.46	5.44	5.42	5.41	5.41	5.39	5.38
Time (s)	538.4	527.9	501.3	503.4	478.8	467.8	468.2

objective, demonstrating that the proposed method can adjust topological features without compromising convergence stability. From Figs. 9(b)-9(f), the number of holes increases to 9 by iteration 19, which violates the prescribed constraint. Subsequently, redundant small holes are eliminated, and by iteration 30, adjacent void regions merge through local structural reconfiguration, reducing the hole count to satisfy $N_1 \leq 4$. A transient isolated component is observed at iteration 30, but it is removed by iteration 43, confirming the effectiveness of the zero-dimensional objective in enforcing global connectivity.

4.3. Cantilever beam example

In this subsection, the classic cantilever beam is considered. The beam length is three times its width. The boundary conditions are shown in Fig. 10(a): the left boundary is fixed, while a downward force of 10^6 is applied at the midpoint of the right boundary. The prescribed volume fraction is set to 0.4. In the IGA model, a bi-quadratic NURBS surface is employed to represent both the design domain and density field. The number of control points in this model is 101×51 , with 4704 elements.

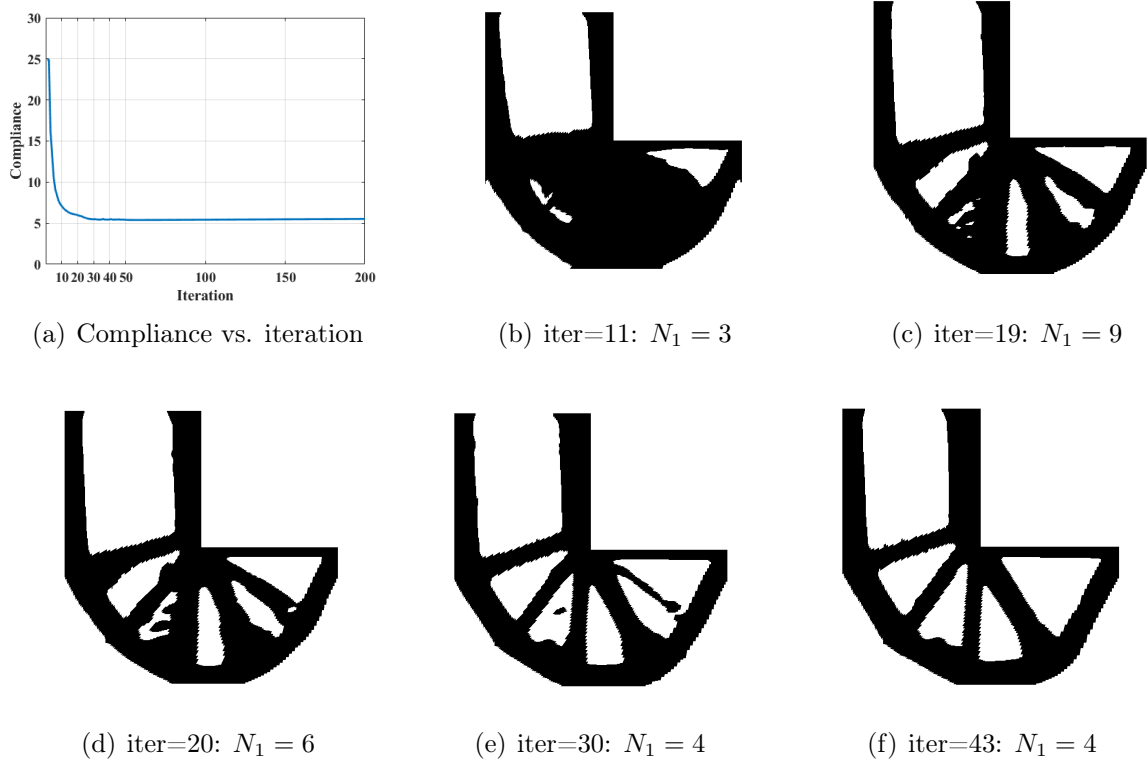


Figure 9: Evolution of the optimized topology for the L-shaped beam when $\bar{N}_1 = 4$. Density fields at representative iterations are shown.

As shown in Figs. 10(b) and 10(c), there exist 6 holes in the optimized structure without topological control.

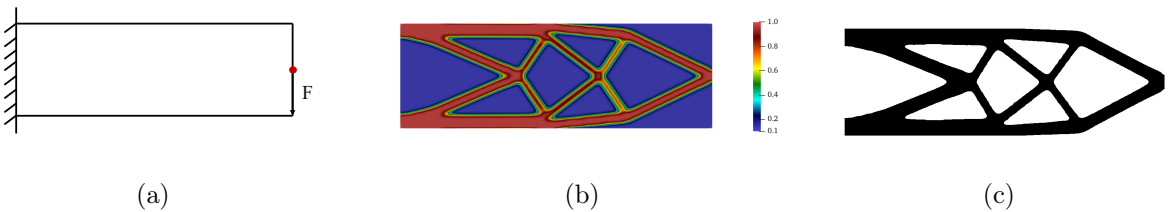


Figure 10: (a) Cantilever beam model. (b) Optimization result without topology control. (c) Binary structure corresponding to the density field in (b).

Fig. 11 and Table 3 summarize the topology-controlled results for $\bar{N}_1 = 1, 2, 3, 4, 5, 6, 7$. Overall, reducing the allowable number of holes leads to a moderate compliance increase, consistent with the reduced admissible design space under stronger topological constraints. Notably, the unconstrained solution exhibits a symmetric layout (Fig. 10(c)). After topology control is imposed, the optimized designs may become non-symmetric. This behavior is

expected: topological constraints can break symmetry by restricting admissible void configurations, even when the loading and boundary conditions are symmetric. Importantly, the resulting designs remain mechanically sound and satisfy the prescribed topology.

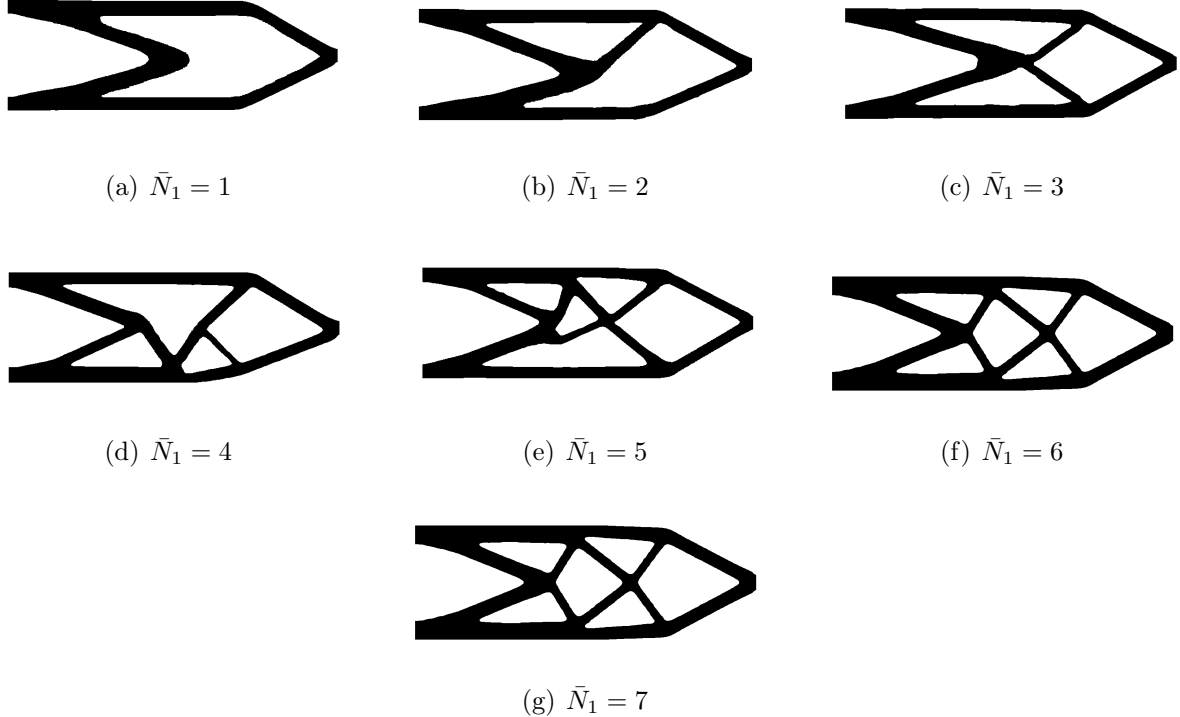


Figure 11: Optimization results of the cantilever beam for $\bar{N}_1 = 1, 2, 3, 4, 5, 6, 7$, respectively.

Table 3: Comparison of compliance, number of holes, and time costs for the cantilever beam benchmark under different topology-control settings.

	$\bar{N}_1 = 1$	$\bar{N}_1 = 2$	$\bar{N}_1 = 3$	$\bar{N}_1 = 4$	$\bar{N}_1 = 5$	$\bar{N}_1 = 6$	$\bar{N}_1 = 7$
weights (μ_0, μ_1)	(1.1,0.9)	(1.1,0.9)	(1.0,0.8)	(0.9,0.7)	(0.9,0.7)	(0.4,0.2)	(0.4,0.2)
Compliance	17.5	17.3	17.1	16.1	16.5	15.9	15.9
Time (s)	553.8	539.7	306.1	231.1	146.5	283.1	285.2

Fig. 12 illustrates the optimization process with topology control $\bar{N}_1 = 3$. In the early iterations, the structure tends to generate holes and additional connected components, as the compliance dominates the objective function at this stage. Fig. 12(a) shows that the compliance exhibits significant variation during the first 20 iterations, indicating that the main structure skeleton is formed during this stage. Subsequently, the compliance becomes nearly stable as iterations proceed, with this phase primarily focused on optimizing the number of holes. At the 17th iteration, the structure exhibits 5 connected components and

2 holes; at the 20th iteration, 12 holes appear in the structure. After activating topology control at iteration 30, redundant small holes disappear rapidly and local structural reconfigurations (including the removal of ineffective thin members) drive the design toward the prescribed hole constraint. Specifically, the hole number decreases from 8 at iteration 30 to 3 at iteration 38, satisfying $N_1 \leq 3$. The compliance remains nearly constant during this topology-correction stage, demonstrating that the proposed persistence-based objective regulates topology without inducing numerical instability.

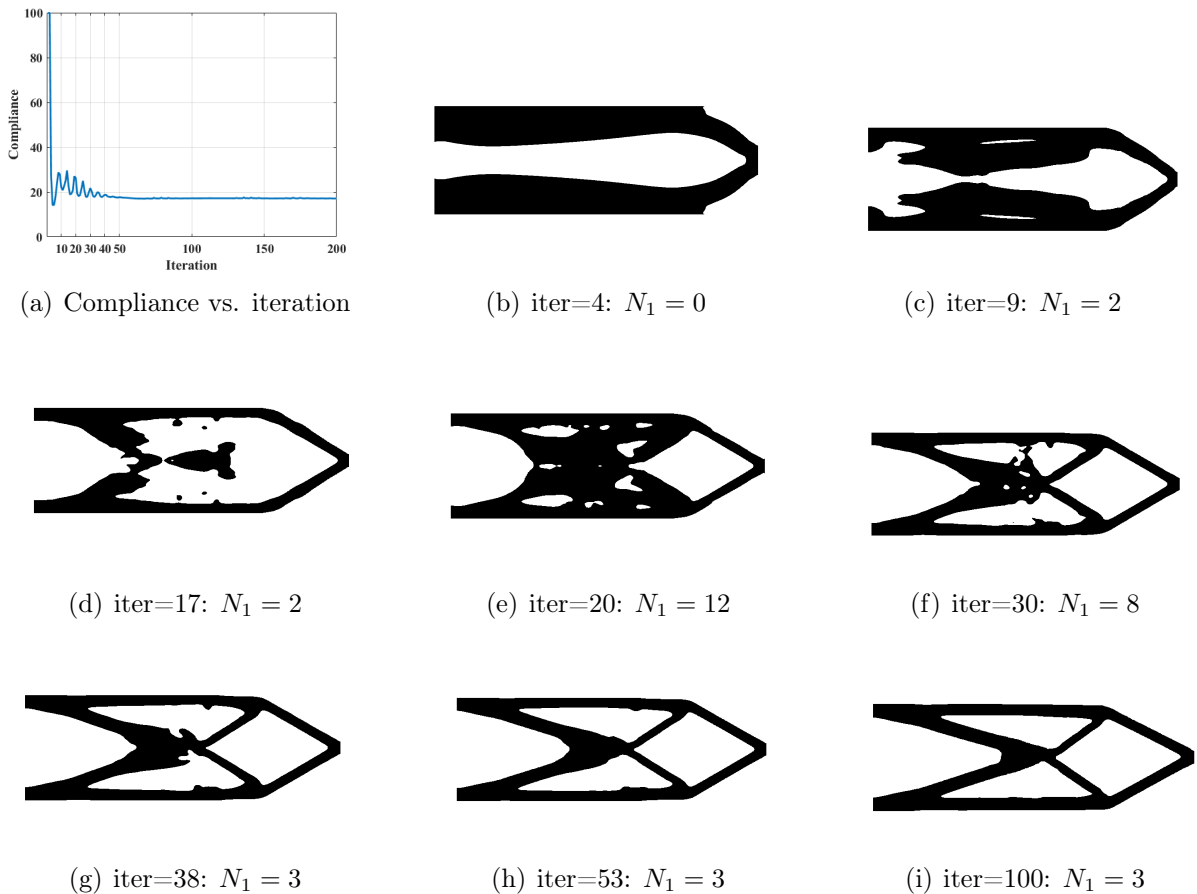


Figure 12: Evolution of the optimized topology for the cantilever beam when $\bar{N}_1 = 3$. Density fields at representative iterations are shown.

Fig. 13(a) shows a typical situation where the hole-number constraint is satisfied, yet a small amount of excess material remains. Although this material contributes marginally to stiffness, it may persist due to the coupling between compliance minimization and the topology objective. To remove such ineffective material while preserving the achieved topology, we freeze the density values within the identified holes and continue optimizing compliance for the remaining design region. As shown in Fig. 13(b), the excess material is progressively eliminated with negligible impact on structural performance. In Fig. 13(a), the compliance of the structure is 17.4, and the compliance in Fig. 13(b) is 17.3. This post-processing step

improves manufacturability while maintaining both topology constraints and mechanical efficiency.

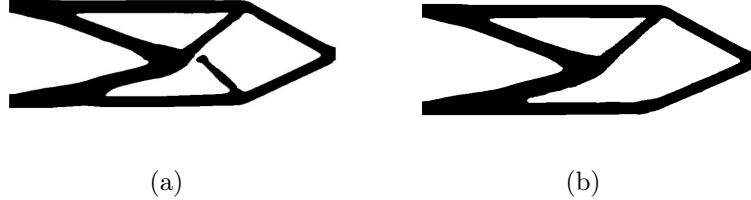


Figure 13: (a) Optimized structure with excess material. (b) Optimized structure after removing excess material.

4.4. Quarter annulus example

In this subsection, we consider a quarter annulus with inner radius $r = 5$ and outer radius $R = 10$, as shown in Fig. 14(a). The bottom boundary of the design domain Ω is fully fixed, and a downward load of 10^6 is applied at the top-right tip of Ω . The prescribed volume fraction is set to $V_0 = 0.4$. Both the design domain Ω and density field are represented by NURBS bases of degree 2. The discretization employs 62×62 control points and 3600 elements. With IGA, the exact geometric representation is maintained throughout the analysis and optimization.

As shown in Figs. 14(b) and 14(c), there exist 3 holes in the optimized structure without topological control.

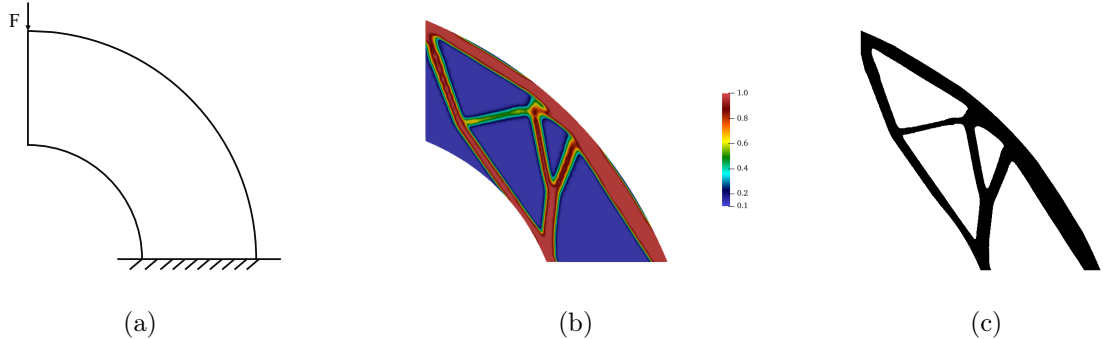


Figure 14: (a) Quarter annulus model. (b) Optimization result without topology control. (c) Binary structure corresponding to the density field in (b).

Fig. 15 and Table 4 summarize the topology-controlled results for $\bar{N}_1 = 1, 2, 3, 4$. A similar performance-complexity trade-off is observed. The compliance increases as the allowable number of holes decreases. The optimization process for $\bar{N}_1 = 1$ is shown in Fig. 16. In Figs. 16(d) and 16(e), it can be observed that there exists 4 holes in the structure at

26th iteration. After only one iteration, the hole number drops to 1 as small topological features are rapidly suppressed, demonstrating the strong corrective capability of the proposed topology objective.

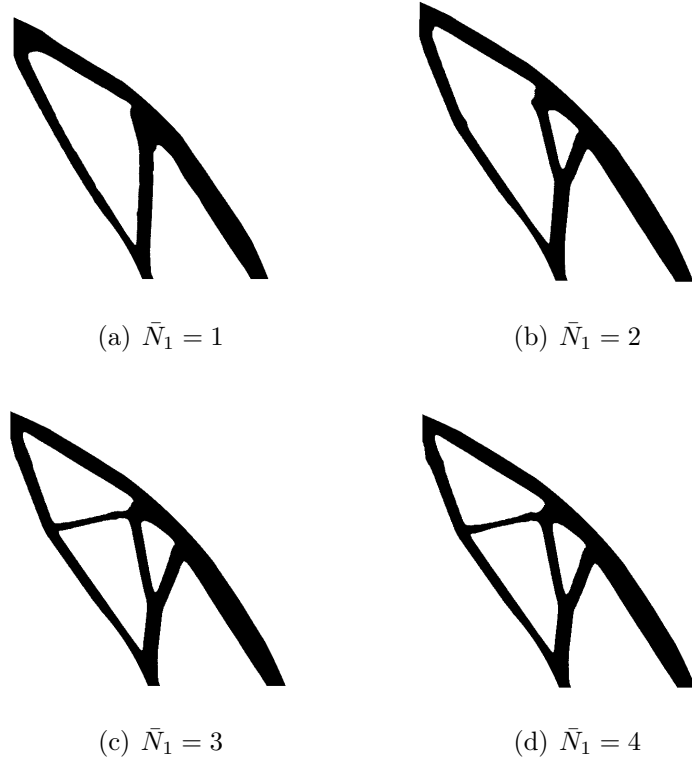


Figure 15: Optimization results of the quarter annulus for $\bar{N}_1 = 1, 2, 3, 4$, respectively.

Table 4: Comparison of compliance, number of holes, and time costs for the quarter annulus model benchmark under different topology-control settings.

	$\bar{N}_1 = 1$	$\bar{N}_1 = 2$	$\bar{N}_1 = 3$	$\bar{N}_1 = 4$
weights (μ_0, μ_1)	(0.4,0.3)	(0.1,0.05)	(0.05,0.05)	(0.05,0.05)
Compliance	10.9	10.7	10.5	10.5
Time (s)	271.3	122.6	189.2	172.9

5. Conclusion

In this work, we present a persistent-homology-based framework for explicit topology control within density-based topology optimization. By incorporating persistence diagrams into the optimization process, both structural connectivity and the number of holes are rigorously quantified and explicitly regulated. The resulting topology-aware objective is fully

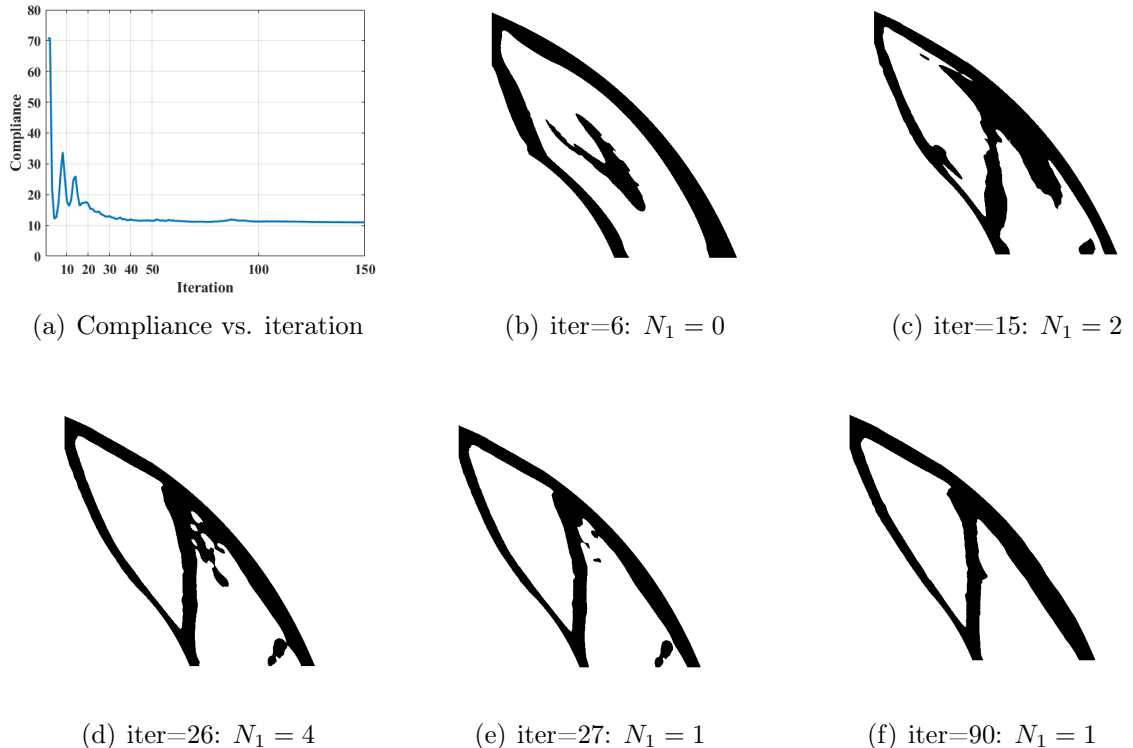


Figure 16: Evolution of the optimized topology for the quarter annulus when $\bar{N}_1 = 1$. Density fields at representative iterations are shown.

differentiable and can be seamlessly integrated into gradient-based solvers, such as MMA. Through a series of benchmark examples, we demonstrate that the proposed method achieves explicit and reliable topology regulation while maintaining competitive mechanical performance and stable convergence behavior. Compared with conventional implicit strategies, the present framework establishes a direct correspondence between design variables and topological features, thereby providing a systematic and mathematically grounded mechanism for controlling structural complexity. Although the current study focuses on two-dimensional problems, the proposed formulation is naturally extensible to three-dimensional settings. Future work will investigate large-scale three-dimensional applications, improve computational efficiency for high-resolution discretizations, and explore strategies for enforcing fully hole-free optimized structures when required by manufacturing constraints.

Acknowledgements

References

Bendsøe, M.P., Kikuchi, N., 1988. Generating optimal topologies in structural design using a homogenization method. *Computer methods in applied mechanics and engineering* 71, 197–224.

Bourdin, B., 2001. Filters in topology optimization. *International journal for numerical methods in engineering* 50, 2143–2158.

Brüel-Gabrielsson, R., Ganapathi-Subramanian, V., Skraba, P., Guibas, L.J., 2020. Topology-aware surface reconstruction for point clouds, in: *Computer graphics forum*, Wiley Online Library. pp. 197–207.

Carriere, M., Chazal, F., Glisse, M., Ike, Y., Kannan, H., Umeda, Y., 2021. Optimizing persistent homology based functions, in: *International conference on machine learning*, PMLR. pp. 1294–1303.

Clough, J.R., Byrne, N., Oksuz, I., Zimmer, V.A., Schnabel, J.A., King, A.P., 2020. A topological loss function for deep-learning based image segmentation using persistent homology. *IEEE transactions on pattern analysis and machine intelligence* 44, 8766–8778.

Edelsbrunner, H., Harer, J., 2010. *Computational topology: an introduction*. American Mathematical Soc.

Han, H., Guo, Y., Chen, S., Liu, Z., 2021. Topological constraints in 2d structural topology optimization. *Structural and Multidisciplinary Optimization* 63, 39–58.

Li, Q., Chen, W., Liu, S., Fan, H., 2018. Topology optimization design of cast parts based on virtual temperature method. *Computer-Aided Design* 94, 28–40.

Liu, S., Li, Q., Chen, W., Tong, L., Cheng, G., 2015. An identification method for enclosed voids restriction in manufacturability design for additive manufacturing structures. *Frontiers of Mechanical Engineering* 10, 126–137.

Piegl, L., Tiller, W., 2012. *The NURBS book*. Springer Science & Business Media.

Poulenard, A., Skraba, P., Ovsjanikov, M., 2018. Topological function optimization for continuous shape matching, in: *Computer Graphics Forum*, Wiley Online Library. pp. 13–25.

Sigmund, O., 1994. Design of material structures using topology optimization. Ph.D. thesis. Technical University of Denmark Lyngby.

Sigmund, O., Petersson, J., 1998. Numerical instabilities in topology optimization: a survey on procedures dealing with checkerboards, mesh-dependencies and local minima. *Structural optimization* 16, 68–75.

Svanberg, K., 1987. The method of moving asymptotes—a new method for structural optimization. *International journal for numerical methods in engineering* 24, 359–373.

Wang, M.Y., Wang, X., Guo, D., 2003. A level set method for structural topology optimization. *Computer methods in applied mechanics and engineering* 192, 227–246.

Yamada, T., Noguchi, Y., 2022. Topology optimization with a closed cavity exclusion constraint for additive manufacturing based on the fictitious physical model approach. *Additive Manufacturing* 52, 102630.

Zhang, W., Liu, Y., Wei, P., Zhu, Y., Guo, X., 2017a. Explicit control of structural complexity in topology optimization. *Computer Methods in Applied Mechanics and Engineering* 324, 149–169.

Zhang, W., Zhou, J., Zhu, Y., Guo, X., 2017b. Structural complexity control in topology optimization via moving morphable component (mmc) approach. *Structural and Multidisciplinary Optimization* 56, 535–552.

Zhao, Z.L., Zhou, S., Cai, K., Xie, Y.M., 2020. A direct approach to controlling the topology in structural optimization. *Computers & Structures* 227, 106141.

Zhou, M., Lazarov, B.S., Wang, F., Sigmund, O., 2015. Minimum length scale in topology optimization by geometric constraints. *Computer Methods in Applied Mechanics and Engineering* 293, 266–282.

Zuo, T., Wang, C., Han, H., Wang, Q., Liu, Z., 2022. Explicit 2d topological control using simp and mma in structural topology optimization. *Structural and Multidisciplinary Optimization* 65, 293.